Journal of Solid State Chemistry **154,** 542–550 (2000)
doi:10.1006/jssc.2000.8877, available online at http://www.idealibrary.com on IDEAL®

An Unusual Metallic Nitride: Sr_2NiN_2

Glen R. Kowach,[1] N. E. Brese,[2] U. M. Bolle,[3] C. J. Warren,[4] and F. J. DiSalvo[5]

Cornell University, Department of Chemistry, Baker Laboratory, Ithaca, New York 14853

Received April 11, 2000; in revised form April 20, 2000; accepted July 17, 2000; published online September 30, 2000

The synthesis of single crystals of Sr_2NiN_2 has been accomplished in a liquid sodium flux from strontium or strontium nitride, nickel, and sodium azide. The decomposition of sodium azide provides additional nitrogen for the synthesis. The structure of Sr_2NiN_2 is derived from the Na_2HgO_2 structure type. However, Sr_2NiN_2 forms with a twinned superstructure. Single crystal X-ray diffraction was used to determine the structure of the tetragonal subcell: *I*4/*mmm*, $a = 3.8874(3)$ Å, $c = 13.992(2)$ Å, $Z = 2$, $R(F) = 5.2\%$, and $R_w(F) = 5.0\%$ with the Ni and N positions split into two sites, each half occupied. The superstructure can be modeled as a $2 \times 1 \times 1$ ordering of the subcell in *Pnma*. The physical properties are unusual since Sr_2NiN_2 displays metallic conductivity and Pauli paramagnetism even though it is comprised of isolated NiN_2 units. In addition, Sr_2NiN_2 possesses a Ni^{2+} formal charge, whereas the oxidation states for nickel nitrides are typically Ni^+ and Ni^0. © 2000 Academic Press

Key Words: **liquid sodium; flux crystal growth; nitride; twinning; superstructure.**

INTRODUCTION

Probing the metal–insulator boundary in materials has revealed interesting phenomena, such as charge density waves, colossal magnetoresistance, and superconductivity (1). In an effort to discover noncuprate superconductors, late transition metal nitrides were synthesized and their electronic and magnetic properties characterized (2). An emphasis was placed on nickel nitrides for several reasons (3): Ni^+ has an electronic configuration (d^9) similar to Cu^{2+} in cuprate superconductors, Ni–N bonding may be similar to Cu–O bonding (combined cation and anion character at the Fermi level), and metallic conductivity was previously observed in CaNiN (4).

Metallic conductivity has been observed in one-, two-, and three-dimensional nitride structures. $LiMoN_2$ was the first layered nitride to demonstrate metallic properties which are attributed to the covalent character of the MoN_2 layers (5,6). Likewise, $CaTaN_2$ exhibits a low resistivity of 0.015 Ω·cm in polycrystalline form at room temperature, and furthermore, it becomes superconducting at approximately 9 K (7). A topotatic insertion of sodium into Ta_3N_5 has led to the conducting solid solution, $Na_xTa_3N_5$ (8). In addition, related mixed-metal nitrides, with structurally similar layers, such as $MMoN_2$ and MWN_2 (M = Fe, Mn, Co, Ni), have been shown to behave as poor metals (9,10). Several nitrides with one-dimensional (1D) extended structures also demonstrate metallic properties, as in CaNiN, which consists of linear $NiN_{2/2}$ chains (4). The highly covalent bonding in these chains leads to short M–N bond distances and a dominating 1D contribution in the electronic structure (11). Metallic properties have also been observed for kinked $NiN_{2/2}$ chains in the SrNiN structure (12).

Solid state compounds with isolated anions, however, typically behave as Mott insulators. Isolated, linear, two-coordinate anions (MN_2^{x-}) are a common motif in ternary late-transition metal nitrides. A survey of these compounds has been previously described (13). The most common oxidation state in nickel nitrides is Ni^+, as seen in the ANiN (A = Ca, Sr, Ba) compounds (4,12,14). However, Ni^0 is observed along with Ni^+ in $Ba_8Ni_6N_7$ (15) and $Li_3Sr_3Ni_4N_4$ (16). Recently Ni^{2+} has been reported for LiNiN (17). Previous research into late transition metal nitride materials revealed anti-ferromagnetic properties for $Sr_{39}Co_{12}N_{31}$, suggesting characteristics of a Mott insulator (13). Surprisingly, the title compound, Sr_2NiN_2, demonstrates metallic electronic character and Pauli paramagnetism even though both $Sr_{39}Co_{12}N_{31}$ and Sr_2NiN_2 structurally consist of isolated nitridometallate anions, thus identifying the proximity of a metal–insulator boundary. In addition, Sr_2NiN_2 has a formal Ni^{2+} cation. This paper describes the synthesis, X-ray diffraction studies, and electrical and magnetic properties of Sr_2NiN_2.

[1] Current address: Lucent Technologies, Bell Laboratories, Murray Hill, NJ 07974.

[2] Current address: Rohm and Haas, Spring House, PA 19477.

[3] Current address: Johannes Gutenberg-Universität, Mainz, 55099 Germany.

[4] Current address: Corning Inc., Corning, NY 14892.

[5] To whom correspondence should be addressed. Fax: (607) 255-4137. E-mail: fjd3@cornell.edu.

0022-4596/00 $35.00

EXPERIMENTAL

Synthesis

All manipulations were carried out in an inert atmosphere (argon) glove box because of the moisture sensitivity of the reactants and nitride products.

A Sr_2N–SrN mixture was prepared by heating strontium metal (rods, 98%, Strem) in an alumina boat positioned inside of a fused silica tube lined with titanium foil. Due to the high vapor pressure of the strontium at 850°C, the fused silica tube must be protected with titanium foil to avoid an oxide impurity in the Sr_2N–SrN mixture. Flowing nitrogen gas (approximately 60 sccm) was purified over heated titanium getters. The reaction of N_2 with Sr is initiated by heating at 475°C for 8 h and slowly raising the temperature to 850°C for an additional 8 h. The resulting stoichiometry is $Sr_{3.4}N_2$ (2.3 Sr_2N:1 SrN ratio). Nitrogen analysis was calculated by the oxidation of the Sr_2N–SrN mixture to SrO; the oxidation was monitored by thermogravimetric analysis (TGA). The brittle strontium nitride product retains the shape of the strontium pieces and is black with a dull luster. The product was identified as Sr_2N (18) by powder X-ray diffraction with most of the observed peaks corresponding to Sr_2N (19), and a shoulder on the peak at $2\theta = 32°$ is observed which matches SrN (20). A discussion of compounds prepared by nitridation of strontium, which includes the stoichiometric assignment of SrN, is provided elsewhere (21).

Strontium azide, $Sr(N_3)_2$, was prepared by following a procedure described in the literature (22). The preparation was accomplished in air because the $Sr(N_3)_2$ is not air or water sensitive. Hydrazoic acid (HN_3) was prepared *in situ* by the dropwise addition of 50 mL of sulfuric acid (0.18 M) into a solution of 0.5414 g of sodium azide (NaN_3, Aldrich, 99%) in 15 mL of distilled water. After addition, the round-bottomed flask was slowly heated until all the HN_3 had distilled into a receiver containing 1.022 g of hydrated strontium hydroxide ($Sr(OH)_2 \cdot 8H_2O$, AESAR, tech. grade) as a suspension in about 30 mL of distilled water. The $Sr(OH)_2$ was made to be the limiting reagent, so that upon losses during the distillation, the final product would be free of unreacted $Sr(OH)_2$. After completing the distillation, the water from the receiving flask was evaporated with the aid of a rotary evaporator, and the white powder was dried in a dessicator under a partial vacuum at room temperature for about 2 days. After the powder was dried, it was stored in the glove box. Powder X-ray diffraction identified the product to be single-phase $Sr(N_3)_2$ (23).

Sr_2NiN_2 single crystals were prepared from nickel powder (submicrometer, 99.8%, Aldrich, purified by heating at 300°C for 12 h in an atmosphere of H_2 and Ar), NaN_3 (99%, Aldrich), and either strontium (rods, 98%, Strem) or the Sr_2N–SrN mixture in sodium (lump, 99%, Aldrich) sealed in a nickel ampoule (seamless tubing, o.d. $\frac{3}{8}$ in.; wall thickness, 0.028 in.; length, approx. 4 in.; min. 99%, Specialty Steel and Forge, etched with 6 M nitric acid). Greater yields were achieved when the Sr_2N–SrN mixture was the starting material. The initial molar ratios were 2 Sr:1 Ni:2 N:5 Na (e.g., reaction number 2.5: 0.2480 g Sr_2N–SrN, 0.0717 g Ni, 0.0194 g NaN_3, 0.1409 g Na). In later syntheses, a slight nitrogen excess was used to promote complete reaction. The nickel ampoules, which were protected in evacuated fused silica reaction tubes, were heated in a box furnace in the upright position. The temperature was increased from room temperature to 900°C over 12 h. After soaking at 900°C for 48 h the tubes were cooled to 500°C over 96 h, whereafter the furnace was turned off. The tubes were opened inside the glove box and then washed three times with approximately 15 mL of liquid ammonia to remove the sodium flux and any unreacted strontium, as previously described (13).

Single phase powder was made by leaching nickel from the reaction tube (6 to 8 cm in length) by heating approximately 80 mg of the Sr_2N–SrN mixture and 20 mg of $Sr(N_3)_2$. The integrity of the container is limited by the pressure of N_2 generated by the decomposition of $Sr(N_3)_2$ (assuming complete decomposition of only the azide, the N_2 pressure would be approximately 12 atm for the above amounts at 1000°C). The nickel tubes, which were protected inside an evacuated fused silica tube, were placed in the furnace horizontally. The furnace was heated to 1000°C for 96 h and then slowly cooled to 500°C over 48 h. The product formed along the walls of the container; it had a color similar to that of the product from the single crystal synthesis. The crystal quality was poor, but the yield was nearly quantitative.

Microscopy

A photomicrograph (Fig. 1) taken with a scanning electron microscope (JEOL 733) illustrates rectangular prismatic morphology of a Sr_2NiN_2 crystal grown from the liquid sodium flux. The electron microscope was equipped with a NORAN 5500 energy dispersive spectrometer (EDS) which was used to evaluate elemental composition. Additionally, a golden metallic luster can be observed with specularly reflected light from the surface of Sr_2NiN_2 crystals. Twin domains are visible in the photomicrograph (Fig. 2) viewed with reflected light under crossed polarizers using an optical microscope. The microcrystalline domain size is approximately 1×10 μm (the third dimension cannot be determined from the photograph).

X-ray Diffraction

Ordinary X-ray diffraction precession photographs taken on an Enraf-Nonius Diffractis 601 diffractometer (Mo$K\alpha$, 45 kV, 15 mA) suggested a small tetragonal unit cell ($a = 3.88$ Å, $c = 14.00$ Å). However, long exposure times

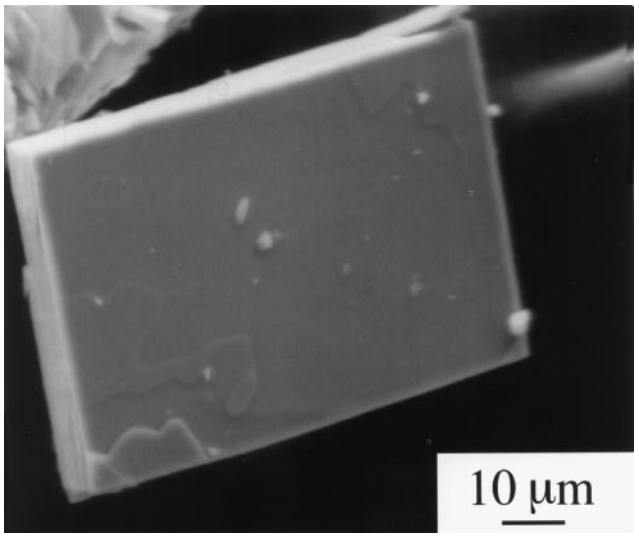

FIG. 1. SEM image of a single crystal of Sr_2NiN_2.

revealed the presence of weak superlattice reflections corresponding to doubling of the *a* and *b* axes.

A black crystal of Sr_2NiN_2 with rectangular prismatic habit bounded by the ± 100, ± 010, ± 001 faces was sealed in a thin-walled glass capillary. The X-ray diffraction data for the $a = 3.8874(3)$ Å and $c = 13.992(2)$ Å subcell were collected on a Rigaku AFC7R diffractometer with graphite monochromated Mo$K\alpha$ ($\lambda = 0.71069$ Å) radiation generated from a rotating anode at 50 kV and 250 mA. Crystallographic details are presented in Tables 1–3. Cell constants, which were obtained from 11 centered reflections in the range $11 < 2\theta < 33^\circ$, indicate a tetragonal unit cell. The Laue check for tetragonal symmetry (four-fold axis parallel to *c*, *R*-merge = 5.3% after empirical absorption correction) was passed by comparing the above symmetry

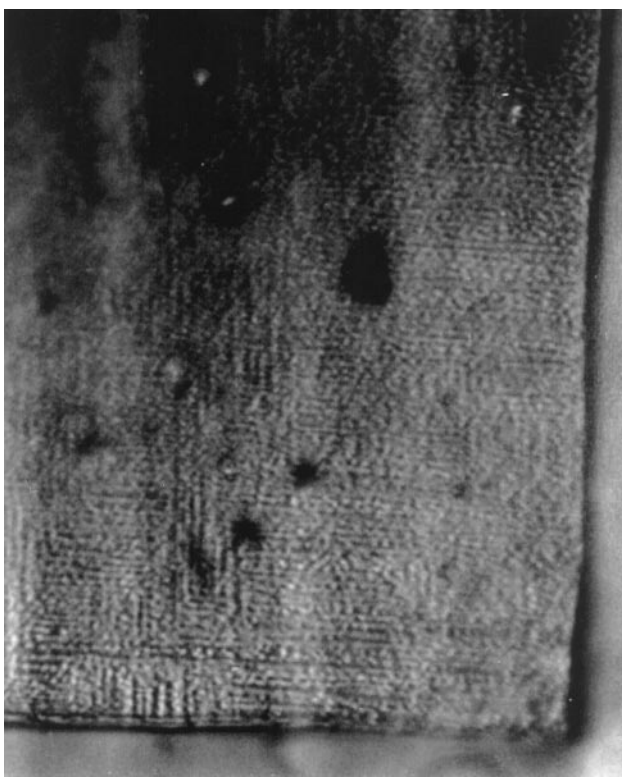

FIG. 2. Photomicrograph viewed with reflected light under crossed polarizers demonstrating the effect of transformation twinning. The viewing area is approximately 40×60 μm.

TABLE 1
Crystallographic Information for Sr_2NiN_2 Subcell

Empirical formula	Sr_2NiN_2
Formula weight	261.95 g/mol
Diffractometer type	Rigaku AFC7R
Monochromator	Graphite
Scan type	$\omega - 2\theta$
Temperature	291(3) K
Wavelength	Mo$K\alpha$
Crystal system	Tetragonal
Space group	*I*4/*mmm* (No. 139)
Unit cell parameters	$a = 3.8874(3)$ Å, $c = 13.992(2)$ Å
Volume	211.47(4) Å^3
Z	2
Density (calculated)	4.102 g/cm^3
Absorption coefficient	292.4 cm^{-1}
F (000)	118
Crystal size	$60 \times 80 \times 20$ μm
Crystal color and habit	Black rectangular prism
2θ Range	$5^\circ < 2\theta < 60^\circ$
Reflections collected	400
Refinement method	Direct methods (SAPI90)
Data/parameters	149/11
Absorption correction	Empirical ψ scans
Normalized transmission factors	0.36 to 1.00
Extinction coefficient	1.3604×10^{-7}
Goodness-of-fit	3.83
Final *R* indices [$I > 3\sigma(I)$]	$R(F) = 5.2\%$, $R_w(F) = 5.0\%$
Maximum peak in diff. map	4.11 e$^-$/Å^3
Minimum peak in diff. map	-2.85 e$^-$/Å^3

Note. $R(F) = \sum||F_o| - |F_c||/\sum|F_o|$ and $R_w(F) = \sum[w||F_o| - |F_c||^2/\sum w|F_o|^2]^{1/2}$, where $w = 1/\sigma^2$.

TABLE 2
Structural Data for Sr_2NiN_2 Subcell

Atom	Wyckoff position	*x*	*y*	*z*	Occupancy	B_{eq}
Sr	4e	0	0	0.6474(2)	1	2.23(3)
Ni	4e	0	0	0.0277(3)	0.5	1.67(6)
N(1)	4e	0	0	0.142(2)	0.5	1.2
N(2)	4e	0	0	0.176(2)	0.5	1.2(3)

Note. $B_{eq} = 8/3\ \pi^2(U_{11}(aa^*)^2 + U_{22}(bb^*)^2 + U_{33}(cc^*)^2 + 2U_{12}aa^*bb^* \cos\gamma + 2U_{13}aa^*cc^* \cos\beta + 2U_{23}bb^*cc^* \cos\alpha)$.

TABLE 3
Anisotropic Displacement Parameters for Sr_2NiN_2 Subcell

	U_{11}	U_{22}	U_{33}	U_{12}	U_{13}	U_{23}
Sr	0.0194(8)	0.0194	0.046(2)	0	0	0
Ni	0.020(2)	0.020	0.023(3)	0	0	0

Note. The anisotropic displacement factor expression is as follows: $\exp(-2\pi^2(a^{*2}U_{11}h^2 + b^{*2}U_{22}k^2 + c^{*2}U_{33}l^2 + 2a^*b^*U_{12}hk + 2a^*c^*U_{13}hl + 2b^*c^*U_{23}kl))$.

equivalent reflections of 10 general reflections of the 11 centered reflections. Data was collected in the ($+h$, $+k$, $+l$) octant; all reflections were collected. Based on systematic absences (hkl: $h + k + l \neq 2n$) which reveal a body-centering condition, the centrosymmetric space group was determined to be $I4/mmm$ (No. 139). The intensities of the standard reflections were collected every 150 reflections, and there was no observable decay. The linear absorption coefficient, μ, for Mo$K\alpha$ radiation is 292.4 cm^{-1}. An empirical ψ-scan absorption correction was applied to the data; the minimum and maximum normalized transmission factors range from 0.36 to 1.00 (teXsan format). The data were corrected for Lorentz polarization effects.

The structure was solved by direct methods (SAPI90) (24) followed by least-squares refinement in the teXsan software package (25). Of the 400 reflections collected, 202 were systematically absent due to the body centering condition, and 49 were considered unobserved due to low intensity ($I < 3\sigma(I)$). All heavy atoms were refined anisotropically. The final cycle of the full-matrix least-squares refinement was based on 149 observed reflections and 11 variables leading to a data to parameter ratio of 13.55:1. The maximum shift/error was 0.003 with a goodness-of-fit of 3.83. The residuals after the final cycle were $R(F) = 5.2\%$ and $R_w(F) = 5.0\%$ with the maximum and minimum peaks in the difference Fourier map of 4.11 and $-2.85\ e^-/Å^3$, respectively. An ORTEP of the unit cell is presented in Fig. 3.

Powder X-ray diffraction was collected on a Scintag XDS 2000 diffractometer with Cu$K\alpha$ ($\lambda = 1.5406$ Å) radiation generated at a tube voltage of 45 kV and current of 40 mA.

TABLE 4
Selected Bond Distances (Å)

Sr	N(2)	2.47(3)
Sr	N(1)	2.749(1)
Sr	N(2)	2.778(4)
Sr	N(1)	2.95(3)
Ni	N(2)	2.07(3)
Ni	N(2)	2.84(3)
Ni	N(1)	2.37(3)
Ni	N(1)	1.59(3)

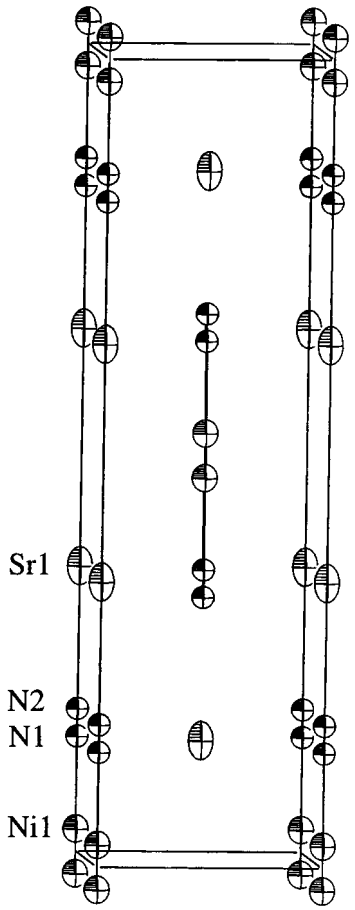

FIG. 3. Clinographic projection of the ORTEP representation of the subcell with split atomic positions for Ni and N.

Physical Property Measurements

The two-probe resistivity was measured by mounting a single crystal of Sr_2NiN_2 on a sapphire plate with two sodium contacts on opposing faces of the crystal (± 100 indexed on tetragonal cell), all manipulations were carried out in a dry box. The contacts were placed so that the current passed in the plane perpendicular to the NiN_2 units. The contacts were ohmic as observed from the I–V characteristic in the applied current range of 34–134 mA. Resistance versus temperature data were taken from 4 to 300 K, using AC lock-in detection at 13 Hz. The resistivity was scaled with the cross-sectional area and inversely with the length of the crystal.

The magnetic susceptibility was measured between 4 and 300 K by utilizing a Faraday balance (26). A 15.9-mg quantity of single phase powder was placed in a Suprasil quartz bucket. Based on field-dependent data, there is a negligible amount of ferromagnetic impurities.

RESULTS AND DISCUSSION

Crystal Growth

Liquid sodium fluxes have been used recently to synthesize many single crystals of binary and ternary nitrides, such as, $Sr_{39}Co_{12}N_{31}$ (13), BaNiN (27), SrCuN and $Sr_6Cu_3N_5$ (28), Sr_2ZnN_2 and Ba_2ZnN_2 (29), $Ba_5Si_2N_6$ (30), $Sr_3Ge_2N_2$ and Sr_2GeN_2 (31), $Ba_3Ge_2N_2$ (32), Ba_2GeGaN and $(Ba_xSr_{1-x})_3Ge_2N_2$ (33), $Ba_3Ga_2N_4$ (34), $Ca_3Ga_2N_4$ (35), and GaN (36,37). Ternary products that have been synthesized in the sodium–alkaline earth flux contain a high alkaline earth content without sodium contamination, thus leading to products usually composed of isolated nitridometallate anions. The crystallization process from the sodium flux is accomplished by the dissolution of nitrogen with the aid of an alkaline earth metal. Presumably, the alkaline earth completes the first coordination sphere around the nitrogen which greatly enhances its solubility (13).

Elemental Analysis

Elemental analysis was performed on single phase material, as observed by powder X-ray diffraction, for strontium and nickel at Galbraith Laboratory by using an inductively coupled plasma (ICP) technique. Excellent agreement was found for Sr_2NiN_2 with 12% Sr_2N as a secondary phase: Calcd.: Sr, 70.0; Ni, 19.7; N, 10.3. Found: Sr, 69.5; Ni, 19.7; and N, 10.8 (N by difference). Although the strontium nitride impurity was not observed by X-ray diffraction, it was visually observed under an optical microscope by exposing the product to air. Strontium nitride is very moisture sensitive and quickly reacts to form strontium hydroxide, whereas the Sr_2NiN_2 is stable in air for several minutes. In order to dismiss oxygen contamination, a modified Dumas method was used to determine the nitrogen content directly by decomposing the Sr_2NiN_2 in molten KOH. This analysis yielded a nitrogen content of 10.3 wt%, in agreement with the ICP data. In addition, EDS analysis indicated that the Sr:Ni ratio was 2:1 within statistical error of 5%.

The products from the liquid sodium flux technique identified by powder X-ray diffraction were nickel and black crystals of Sr_2NiN_2. EDS analysis of a single crystal identified the presence of only strontium and nickel in a 2:1 ratio. Incorporation of the sodium flux was not observed.

Structural Aspects

Subcell. Ordinary X-ray rotation and precession photographs suggest a small tetragonal unit cell. Based on these reflections, a disordered structure was determined from single crystal X-ray diffraction. The model of the subcell is based on the Na_2HgO_2 structure type in space group $I4/mmm$ (38). The Na_2HgO_2 structure, which is isostructural to M_2ZnN_2 compounds, where M is Ca, Sr, or Ba, can be described as rock salt layers of Na and O with Hg atoms bridging the layers and coordinated to the O atoms to form linear HgO_2^{2-} species. Equivalently, it can be described as chains of Na–O–Hg–O–Na running in the [001] direction. The coordination geometry can easily be observed by viewing the structure with polyhedral representations for both cations and anions (Fig. 4). The sodium atoms lie in square pyramidal coordination and the oxygen atoms are bonded to one Hg and five Na atoms in octahedral coordination. For Sr_2NiN_2, the Ni resides about the origin of the unit cell (Fig. 3) in linear coordination with nitrogen. Both the Ni and N are split into two positions at half-occupancy for each with a distance of 0.77 Å between Ni sites. Due to the fact that the splitting of the Ni position is small and that X-ray structure determination only provides a solution for the average structure, only one Ni atom can reside on the disordered Ni site at a time. This leads to two possible models for the Ni–N bonding. The first having one short and one long Ni–N bond and the second having two short Ni–N bonds. The second model is more plausible due to the covalent nature of the Ni–N bond. Given that the N positions are difficult to resolve by X-ray diffraction due to a small scattering cross section, it is likely that the distance between the split N positions would be similar to the splitting between the Ni positions. Although accurate bond distances are difficult to obtain, the Ni–N bond distances in Sr_2NiN_2 are similar to those found in related compounds. Distances for Ni–N bonds in other nickel nitride compounds are as follows: CaNiN 1.79 Å (4); SrNiN 1.83, 1.89 Å (12); BaNiN 1.79 Å, 1.83 Å (14); $Ba_8Ni_6N_7$ 1.75 to 1.81 Å (15); and $Li_3Sr_3Ni_4N_4$ 1.77 Å (16). The Sr–N bond distances are between 2.47 and 2.95 Å, which is typical for Sr nitrides with nitrogen in octahedral coordination. For example, $Li_3Sr_3Ni_4N_4$ has Sr–N bond distances from 2.64 to 2.78 Å and SrNiN 2.45 to 2.89 Å. The closest Ni–Ni distance is 3.89 Å, thereby indicating negligible metal–metal interaction from direct orbital overlap.

Supercell. In an attempt to understand the disordered structure described above, additional experiments were executed to probe for superstructure. Supercell reflections were initially discovered by long exposure precession photographs. The superstructure consists of an ordering of the NiN_2 units by a decrease in symmetry as observed by powder X-ray diffraction and a doubling of the unit cell in at least one direction as observed in reciprocal lattice photographs.

Several reflections, which were observed by powder X-ray diffraction, indicate a reduction in symmetry from the tetragonal symmetry of the subcell. The following reflections displayed good intensity and occurred at large values of 2θ such that the splitting was easily resolved (based on the indexing of the subcell): (124), (200), (211), (404), and (213).

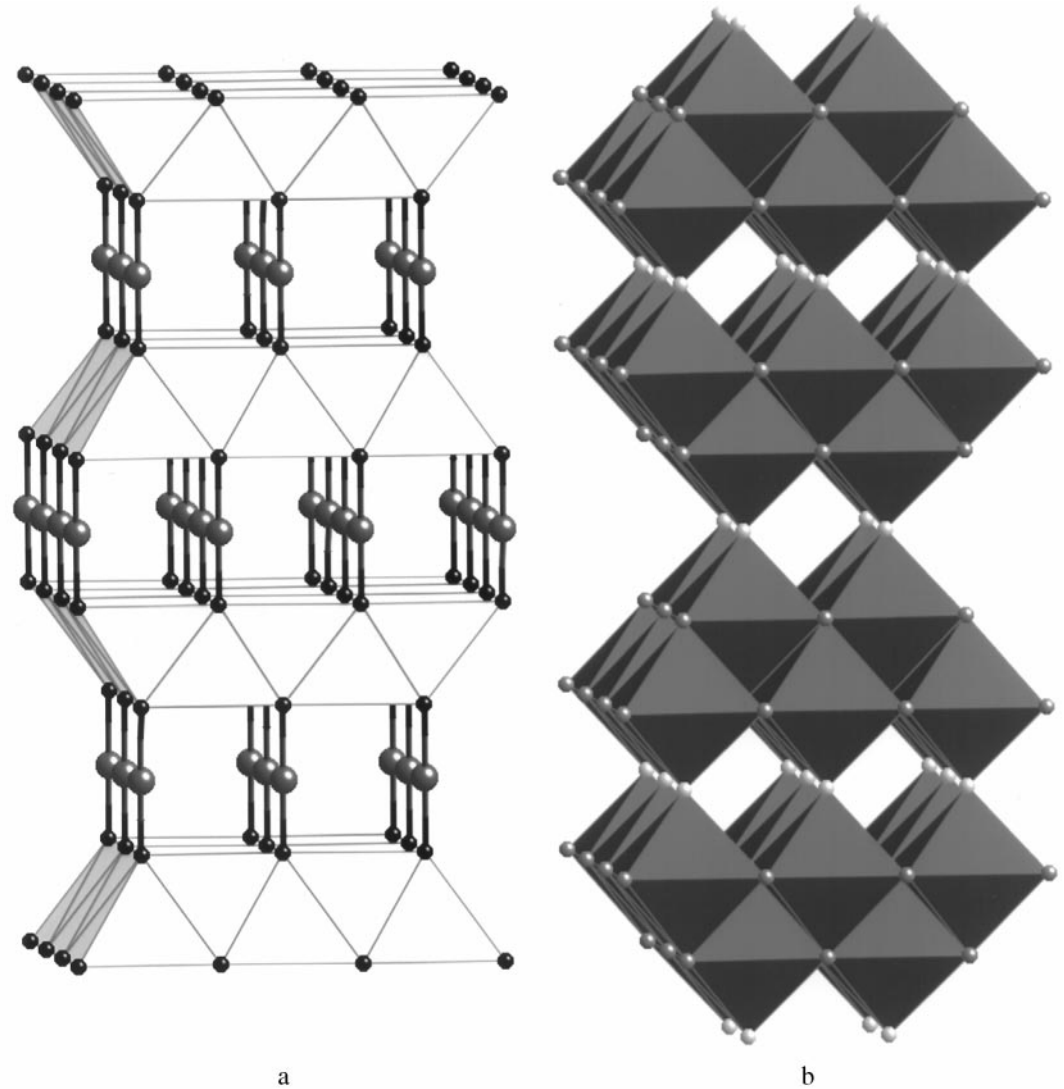

FIG. 4. Polyhedral representation of the Na_2HgO_2 structure type: (a) Na-centered cation square pyramids with Hg as large spheres and O as small spheres and (b) O-centered anion octahedra. In both views the *c*-axis is vertical.

Calculation of the lattice parameters suggest an orthorhombic unit subcell with $a = 3.89$ Å, $b = 3.91$ Å, and $c = 14.00$ Å.

The supercell appears to form a $2 \times 2 \times 1$ superstructure from precession photographs. Based on the indexing of a unit cell with doubled *a* and *b* axes, the supercell reflections observed as follows: in the *h*0*l* and 0*kl* layers (104), (107), (1010), (304), and (307); in the *h*1*l* layer (017), (0110), (214), (217), (2110), (417), and (4110); in the *h*2*l* layer (125), (127), and (327). Additional peaks were not observed in the precession photographs, which would indicate contact twins having an arbitrary contact angle.

The twinning can be described as pseudomerohedral (39) because all diffraction spots were observed on reciprocal lattice points with tetragonal lattice parameters of roughly $a = 8$ Å and $c = 14$ Å. The twinning is not purely merohedral due to the slight distortion to orthorhombic symmetry as observed by powder X-ray diffraction. The twin domains visible by optical microscopy are indicative of transformation twins that result from a phase transition to the distorted state at a temperature between the growth temperature and room temperature.

From these observations and extensive single-crystal X-ray diffraction data described elsewhere (40), the structure can be modeled as an orthorhombic $2 \times 1 \times 1$ ($a = 7.81$ Å, $b = 3.89$ Å, $c = 14.01$ Å) superstructure with twin domains at perpendicular orientations. Idealized atomic positions can be found in Table 5 for *Pnma* symmetry.

This superstructure is illustrated in Fig. 5. By comparing the distorted Sr_2NiN_2 structure to Ca_2ZnN_2, the driving

TABLE 5
Idealized Atomic Positions in *Pnma* for a 2 × 1 × 1 Superstructure

Atom	*x*	*y*	*z*
Sr1	0.125	0.25	0.54
Sr2	0.625	0.25	0.60
Ni	0.125	0.25	0.22
N1	0.125	0.25	0.09
N2	0.125	0.25	0.35

force for lower symmetry, i.e., modulation of the Ni position, may be attributed to electronic interactions in the Ni *d* orbitals which have a d^8 electronic configuration, whereas the Zn has a closed shell d^{10} configuration. Additional analytical techniques are necessary to accurately define the atomic positions of the twinned superstructure.

Physical Properties

The resistance versus temperature data (Fig. 6) surprisingly demonstrates metallic electrical conductivity for Sr_2NiN_2. From the room temperature value ($6 \times 10^{-3}\,\Omega\cdot$cm) and the decrease in resistivity as the sample was cooled, metallic behavior is clearly observed. The room temperature value should be taken as an upper limit due to the two-probe technique in which the contact resistances are included in the measurement.

The metallic behavior of Sr_2NiN_2 was quite unexpected. Given the large Ni–Ni separation, direct overlap of metal *d* orbitals is negligible. Therefore, Sr_2NiN_2 would be expected to be a Mott insulator, which would have a magnetic moment corresponding to any unpaired *d* electrons. Therefore, in order to confirm the electrical properties, magnetic susceptibility was measured.

The temperature-dependent data were fit to Curie-Weiss law, $\chi_g = \chi_0 + C/(T + \theta)$, where χ_g is the measured gram susceptibility, χ_0 is a temperature-independent susceptibility, C is the Curie constant, T is temperature, and θ is the Curie-Weiss constant. The fit to Curie-Weiss law over $70\text{ K} < T < 220\text{ K}$ gave $\theta = 18$ K, $\mu_{\text{eff}} = 0.6$ B.M., and $\chi_0 = 1.04 \times 10^{-7}$ emu g^{-1} ($\sigma_{\text{fit}} = 0.5\%$). The intrinsic character of Sr_2NiN_2 is Pauli paramagnetic (41) as determined by the positive sign and magnitude of the temperature-independent magnetic susceptibility, χ_0. The small effective magnetic moment may possibly be attributed to a 1.6% Fe^{2+} impurity from the nickel tubing.

Thermal cycling shows the onset of a ferromagnetic signal due to Ni from the decomposition of Sr_2NiN_2 as the temperature approaches room temperature. It seems unlikely that thermal cycling alone would affect the sample because Sr_2NiN_2 is stable at room temperature for several months in an inert atmosphere. Perhaps, the decomposition is due

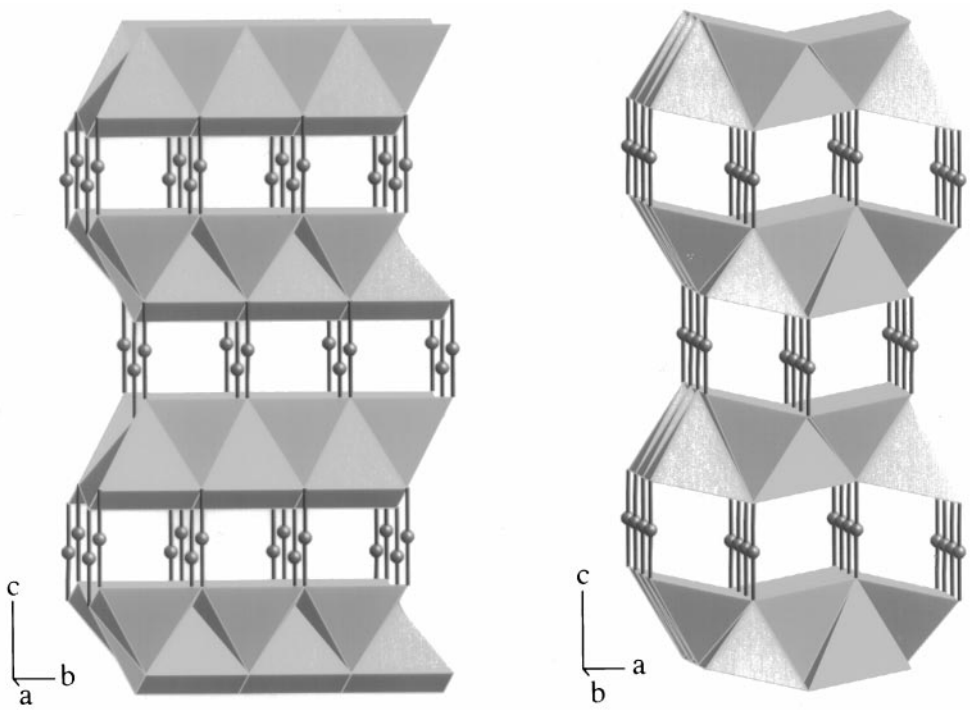

FIG. 5. Two projections for the idealized model in *Pnma* for the superstructure with the NiN_2^{4-} units illustrated with two short Ni–N bonds (1.8 Å). The isolated nitridometallate units are modulated in the [100] direction for the cell indexed by $a = 7.81$ Å, $b = 3.90$ Å, and $c = 14.01$ Å. The distorted square pyramidal polyhedra are centered by Sr, and the Ni atoms are represented by spheres.

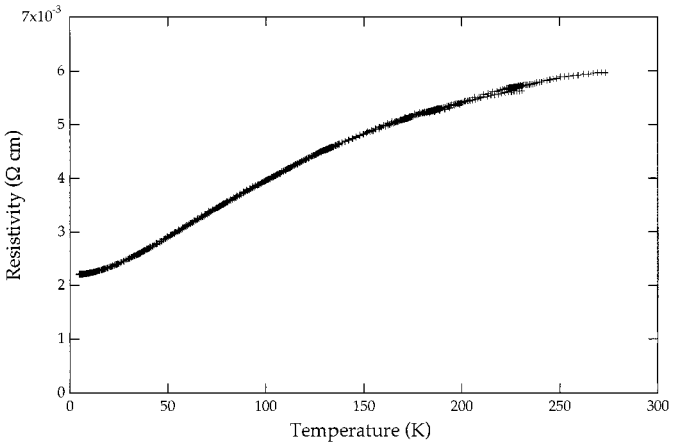

FIG. 6. Temperature-dependent resistivity of Sr_2NiN_2 demonstrating metallic conductivity.

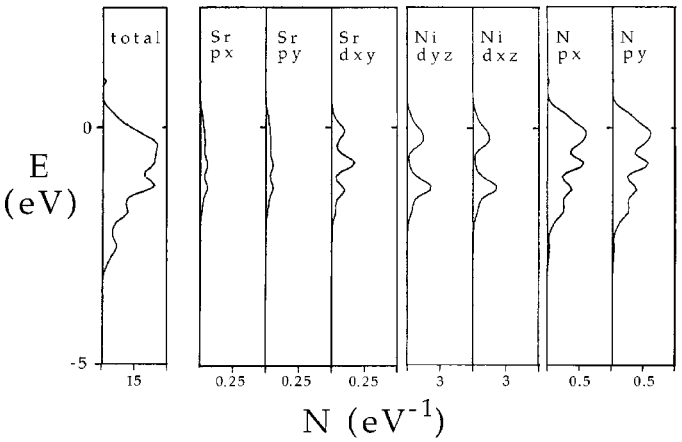

FIG. 7. The electronic band structure of the Sr_2NiN_2 subcell. The axes represent energy (E) referenced to the Fermi level ($E_f = 0$) and density of states (N).

to a slight moisture contamination. This decomposition behavior is also seen in $Sr_{39}Co_{12}N_{31}$ (13). Also, thermal cycling also shows a sharp increase in the resistivity as the temperature approaches room temperature.

Although electrical conductivity in materials with isolated anions is unexpected, it is not unprecedented. An example in the literature of a metallic material with isolated metallate moities is Na_2PdH_2, which is also isostructural to Na_2HgO_2. This compound demonstrates metallic behavior even though the $[PdH_2]^{2-}$ anions are isolated from each other such that there are no direct Pd–Pd interactions (42). To examine the atomic character of the wavefunctions which participate in conductivity of Sr_2NiN_2, band structure calculations were initiated.

Band Structure Calculations

In order to understand the origin of the metallic conductivity, a full-potential linear-muffin-tin-orbital (LMTO) band structure (43) was calculated for the Sr_2NiN_2 subcell. The calculation was simplified by employing the Na_2HgO_2 structural model. The Sr_2NiN_2 subcell band structure (Fig. 7) indicates that the Fermi level (E_f) lies in a band with substantial Ni–d_{yz}, d_{xz} and N–p_x, p_y character as expected, but also with Sr-p and -d orbital mixing as well. A finite density of states at E_f suggests metallic character, and the nonnegligible strontium orbital character in the wavefunctions at E_f provides a pathway for conduction of electrons between the NiN_2 units. These calculations are consistent with the observed properties of Sr_2NiN_2. Mixing of strontium orbitals into the wavefunctions near E_f is necessary to achieve metallic character. Also, strong anion and cation mixing at the Fermi level is observed, which has been suggested as a characteristic of high-temperature superconductors.

CONCLUSIONS

The reproducible synthesis of Sr_2NiN_2 single crystals and single phase powder is described. The tetragonal subcell can be described with $I4/mmm$ symmetry having disordered Ni and N positions. This compound undergoes a transformation into a twinned supercell which can be modeled as a volumetric doubling of the subcell. Sr_2NiN_2 demonstrates unusual metallic conductivity and exhibits Pauli paramagnetism. The discovery of a metallic Ni^{2+} nitride fosters the idea that high temperature superconductivity may be possible in nitrides to which the assignment of formal charge combinations for cuprates (Cu^{3+} d^8, Cu^{2+} d^9) have electron configurations similar to those of nitridonickelates (Ni^{2+} d^8, Ni^{+} d^9).

ACKNOWLEDGMENTS

The authors gratefully acknowledge R. C. Haushalter and the NEC Research Institute for the use of the Rigaku X-ray diffractometer and helpful discussions. B. Hannebauer and P. C. Schmidt are acknowledged for the band structure calculations. We thank D. A. Vennos for her initial work in this area, also M. C. Gelabert, Y. Ijiri, and H. Yamane for help with the resistivity measurements, magnetic susceptibility, and X-ray precession camera work, respectively.

REFERENCES

1. C. Kittel, "Introduction to Solid State Physics," 6th ed., p. 268. Wiley, New York, 1986.
2. F. J. DiSalvo, *Science* **247,** 649 (1990).
3. D. L. Nelson, M. S. Whittingham, and T. F. George (Eds.), "Chemistry of High Temperature Superconductors," ACS Symposium Series No. 351, p. 49. American Chemical Society, Washington, DC, 1987.
4. Ming Y. Chern and F. J. DiSalvo, *J. Solid State Chem.* **88,** 459 (1990).
5. S. H. Elder, L. H. Doerrer, F. J. DiSalvo, J. B. Parise, D. Guyomard, and J. M. Tarascon, *Chem. Mater.* **4,** 928 (1992).

6. D. J. Singh, *Phys. Rev. B* **46,** 9332 (1992).
7. V. E. Balbarin, R. B. van Dover, and F. J. DiSalvo, *J. Phys. Chem. Solids* **57,** 1919 (1996).
8. S. J. Clarke and F. J. DiSalvo, *J. Solid State Chem.* **132,** 394 (1997).
9. H.-C. zur Loye, J. D. Houmes, and D. S. Bem, *in* "The Chemistry of Transition Metal Carbides and Nitrides" (S. T. Oyama Ed.). Blackie Academic and Professional, Glasgow, 1995.
10. P. Subramanya Herle, N. Y. Vasanthacharya, M. S. Hegde, and J. Gopalakrishnan, *J. Alloys Compd.* **217,** 22 (1995).
11. S. Massidda, W. E. Pickett, and M. Posternak, *Phys. Rev. B* **44,** 1258 (1991).
12. T. Yamamoto, S. Kikkawa, and F. Kanamaru, *J. Solid State Chem.* **115,** 353 (1995).
13. G. R. Kowach, H. Y. Lin, and F. J. DiSalvo, *J. Solid State Chem.* **141,** 1 (1998).
14. A. Gudat, S. Haag, R. Kniep, and A. Rabenau, *J. Less-Common Met.* **159,** L29 (1990).
15. A. Gudat, W. Milius, S. Haag, R. Kniep, and A. Rabenau, *J. Less-Common Met.* **168,** 305 (1991).
16. A. Gudat, R. Kniep, and A. Rabenau, *Z. Anorg. Allg. Chem.* **597,** 61 (1991).
17. M. G. Barker, A. J. Blake, D. H. Gregory, D. J. Siddons, S. E. Smith, P. P. Edwards, and T. A. Hamor, *Chem. Commun.* **13,** 1187 (1999).
18. N. E. Brese and M. O'Keeffe, *J. Solid State Chem.* **87,** 134 (1990).
19. Powder Diffraction File, Card No. 25-855, Joint Committee on Powder Diffraction Standards (JCPDS), Swarthmore, PA.
20. Powder Diffraction File, Card No. 25-856, Joint Committee on Powder Diffraction Standards (JCPDS), Swarthmore, PA.
21. N. E. Brese, M. O'Keeffe, *Struct. Bonding* **79,** 307 (1992).
22. P. Ehrlich, *in* "Handbook of Preparative Inorganic Chemistry" (G. Brauer Ed.), Vol. 1, 2nd ed., p. 942, Academic Press, New York, 1963.
23. Powder Diffraction File, Card No. 21-1466, Joint Committee on Powder Diffraction Standards (JCPDS), Swarthmore, PA.
24. F. Hai-Fu, "Structure Analysis Programs with Intelligent Control." Rigaku Corporation, 1990.
25. "Crystal Structure Analysis Package." Molecular Structure Corporation, 1985 & 1992.
26. J. K. Vassiliou, M. Hornbostel, R. Ziebarth, and F. J. DiSalvo, *J. Solid State Chem.* **81,** 208 (1989).
27. G. R. Kowach, unpublished results.
28. F. J. DiSalvo, S. S. Trail, H. Yamane, and N. E. Brese, *J. Alloys Compd.* **255,** 122 (1997).
29. H. Yamane and F. J. DiSalvo, *J. Solid State Chem.* **119,** 375 (1995).
30. H. Yamane and F. J. DiSalvo, *J. Alloys Compd.* **240,** 33 (1996).
31. S. J. Clarke, G. R. Kowach, and F. J. DiSalvo, *Inorg. Chem.* **35,** 7009 (1996).
32. H. Yamane and F. J. DiSalvo, *J. Alloys Compd.* **241,** 69 (1996).
33. S. J. Clarke and F. J. DiSalvo, *J. Alloys Compd.* **259,** 158 (1997).
34. H. Yamane and F. J. DiSalvo, *Acta Crystallogr. C*52, 760 (1996).
35. S. J. Clarke and F. J. DiSalvo, *J. Alloys Compd.* **274,** 118 (1998).
36. H. Yamane, M. Shimada, S. J. Clarke, and F. J. DiSalvo, *Chem. Mater.* **9,** 413 (1997).
37. H. Yamane, M. Shimada, and F. J. DiSalvo, *Mater. Lett.* **42,** 66 (2000).
38. R. Hoppe and H.-J. Röhrborn, *Z. Anorg. Allg. Chem.* **329,** 110 (1964).
39. V. K. Wadhawan and C. Boulesteix, *in* "Diffusionless Phase Transitions and Related Structures in Oxides" (C. Boulesteix, Ed.), p. 71. Trans Tech Publications, Brookfield, VT, 1992.
40. G. R. Kowach, Dissertation, Cornell University, 1997.
41. M. M. Schieber, "Experimental Magnetochemistry" (E. P. Wohlfarth Ed.), p. 10. North-Holland, Amsterdam, 1967.
42. K. Kadir, M. Kritikos, D. Noréus, and A. F. Andresen, *J. Less-Common Met.* **172–174,** 36 (1991).
43. M. Methfessel, *Phys. Rev. B* **38,** 1537 (1988).